

Article

Thermal, Mechanical, and Electrochemical Characterization of $Ti_{50}Ni_{50-x}Mo_x$ Alloys Obtained by Plasma Arc Melting

Josiane D. Costa ^{1,*}, Mikarla B. Sousa ¹, Arthur F. Almeida ¹, José A. M. Oliveira ², Paulo C. S. Silva ²,
José J. N. Alves ¹, Ana R. N. Campos ¹, Carlos J. Araújo ², Renato A. C. Santana ²,
João M. P. Q. Delgado ^{3,*} and Antonio G. B. Lima ²

- ¹ Department of Chemical Engineering, Federal University of Campina Grande, Avenida Aprígio Veloso 882, Campina Grande 58429-970, Brazil; mikarlabaia@hotmail.com (M.B.S.); arthur.filgueira@eq.ufcg.edu.br (A.F.A.); jose.jailson@ufcg.edu.br (J.J.N.A.); ana.regina@professor.ufcg.edu.br (A.R.N.C.)
- ² Department of Mechanical Engineering, Federal University of Campina Grande, Avenida Aprígio Veloso 882, Campina Grande 58429-970, Brazil; jmo.anderson@gmail.com (J.A.M.O.); paulocesarsales@outlook.com (P.C.S.S.); carlos.jose@professor.ufcg.edu.br (C.J.A.); renato.alexandre@professor.ufcg.edu.br (R.A.C.S.); antonio.gilson@ufcg.edu.br (A.G.B.L.)
- ³ Construct-LFC, Civil Engineering Department, Faculty of Engineering, University of Porto, 4200-465 Porto, Portugal
- * Correspondence: josianeeq@gmail.com (J.D.C.); jdelgado@fe.up.pt (J.M.P.Q.D.); Tel.: +351-225081404 (J.M.P.Q.D.)

Abstract: This study aims to manufacture and characterize titanium and nickel alloys with different molybdenum (Ti–Ni–Mo) contents, focusing on the influence of these additions on the microstructure, mechanical properties, and corrosion resistance. The relevance of this work stems from the lack of research on this specific alloy and the absence of reports in the literature with molybdenum percentages above 2 at.%. $Ti_{50}Ni_{50-x}Mo_x$ alloys were produced by the plasma arc melting method, with six different compositions ($x = 0, 0.5, 1, 2, 3,$ and 4 at.% Mo), and a comprehensive analysis of microstructure, chemical composition, thermal, mechanical, and electrochemical properties was carried out. The results demonstrated significant alterations in the microstructure of the Ni–Ti alloy with the addition of molybdenum presenting several phases, precipitates (TiNi, Ti_2Ni), and oxides (Ti_4Ni_2O , TiO, and TiO_3). The stability of the B2 phase increased with molybdenum content, and the monoclinic martensite (B19′) phase was identified only in the Ni–Ti sample. Introducing molybdenum into the Ni–Ti alloy generated the R-phase and shifted the phase transformation peaks to lower temperatures, as differential scanning calorimetry (DSC) indicated. Microhardness and elastic modulus decreased with increasing Mo content, ranging from 494 HV to 272 HV and 74 GPa to 63 GPa, respectively. Corrosion tests revealed increased corrosion resistance with increasing Mo content, reaching a polarization resistance of 2710 $k\Omega \cdot cm^2$ and corrosion current of 11.3 μA . Therefore, this study points to Ti–Ni–Mo alloys as potential candidates to increase the range of Ni–Ti alloy applications, mainly in biomaterials, reinforcing its relevance and need in current alloy research.

Keywords: Ti–Ni–Mo alloys; shape memory alloys; microstructure; microhardness; corrosion



Citation: Costa, J.D.; Sousa, M.B.; Almeida, A.F.; Oliveira, J.A.M.; Silva, P.C.S.; Alves, J.J.N.; Campos, A.R.N.; Araújo, C.J.; Santana, R.A.C.; Delgado, J.M.P.Q.; et al. Thermal, Mechanical, and Electrochemical Characterization of $Ti_{50}Ni_{50-x}Mo_x$ Alloys Obtained by Plasma Arc Melting. *Metals* **2023**, *13*, 1637. <https://doi.org/10.3390/met13101637>

Academic Editors: Ryosuke Kainuma and Alexander V. Shelyakov

Received: 27 June 2023

Revised: 3 August 2023

Accepted: 18 September 2023

Published: 23 September 2023



Copyright: © 2023 by the authors. Licensee MDPI, Basel, Switzerland. This article is an open access article distributed under the terms and conditions of the Creative Commons Attribution (CC BY) license (<https://creativecommons.org/licenses/by/4.0/>).

1. Introduction

There is a class of metallic alloys known as shape memory alloys that are classified as such because they present surprising thermomechanical phenomena such as superelasticity or shape memory effects [1]. These phenomena occur thanks to reversible (thermoelastic) transformations between different crystalline phases, austenite and martensite [2,3]. Austenite has a matrix phase and is stable at higher temperatures, with high symmetry, often of cubic crystalline structure (B2). Martensite is the stable phase at lower temperatures, with less symmetry, often with a monoclinic (B19′), orthorhombic (B19), or rhombohedral (R-phase) structure [1,4].

Within the class of shape memory alloys, the most famous and commercially successful is the Ni–Ti-based alloy family. These alloys exhibit a remarkable shape recovery property, activated upon exposure to heat, stress, or magnetic fields. This characteristic, combined with their adaptability to different load conditions, qualifies these alloys as excellent candidates for applications in actuators and sensors [5], vibration control systems, and for improving the seismic performance of structures [6]. The superelasticity of Ni–Ti alloys additionally enhances their use in various fields of engineering, such as automotive, biomedical [7,8], aerospace, and robotics, as well as in specific industrial applications, including Belleville springs [9], couplings, and cellular antennas [10].

A two-stage transformation sequence ($B2 \rightarrow R \rightarrow B19'$) can be induced in these alloys to obtain desirable responses in specific applications [1]. For example, the hysteresis involved in transforming the Austenite to Martensite phase ($B2 \rightarrow B19'$) is large, around 50 K. In contrast, the transformation from the austenite to martensite phase ($B2 \rightarrow R$) is minimal, making this process desirable for applications such as biomaterials, as they are stable. Furthermore, the small transformation hysteresis means a quick response to an environmental change, an essential aspect of medical applications [11]. However, for the $B2 \rightarrow R$ transformation to be induced, it is necessary for the equiatomic Ni–Ti alloy to undergo some processes as follows: aging of nickel-rich alloys [12–14], thermo-mechanical treatment [15,16], and the addition of a third element such as Fe, Al, Co, or Mo [17–20].

Regarding the addition of a third element, Xi et al. [21] studied the effect of adding Fe on the microstructure, transformation temperatures, and superelasticity of Ni–Ti alloys manufactured by laser melting in a powder bed and found that the addition of Fe distorts the Ni–Ti matrix network, leading to a decrease in martensite transformation temperatures and the appearance of the R-phase. They also observed that the sensitivity of the phase transformation temperature is 10 K for each 0.1 wt.% of Fe added to the alloy. Mohammed et al. [22] evaluated the effect of adding the element cobalt on the characteristics of the equiatomic Ni–Ti alloy with shape memory. They concluded that the thermal hysteresis and the austenitic transformation temperatures decreased with the addition of cobalt while the martensitic transformation temperatures increased. Kim [23] manufactured $Ti_{50}Ni_{49.7}Mo_{0.3}$ fibers and verified that the martensitic transformation occurred in two stages $B2 \rightarrow R \rightarrow B19'$ with the austenite transformation final temperature (34 °C) low enough to present superelasticity at human body temperature.

Ti–Ni–Mo alloys that exhibit shape memory are biomedical materials of great potential thanks to their superior corrosion resistance. Nam et al. [24] highlighted that the corrosion resistance of these alloys surpasses that of pure Ti, commonly applied as an implant material. Posteriorly, Liu et al. [25] manufactured Ti–Ni–Mo alloys by melting arc furnace, varying the molybdenum content to 2.0 at.%. The research showed a notable reduction in the martensite transformation temperatures with the increase in the amount of molybdenum, while the R-phase transformation temperatures showed minimal variation. Analysis of mechanical properties revealed that alloys with higher molybdenum content are promising for applications as coupling devices. Additionally, Kim [26] investigated powders of a Ti–Ni–Mo alloy manufactured by the inert gas atomization process. The results indicated that the alloy with 0.1 at.% molybdenum underwent a phase transformation, in which the martensite phase was observed in two stages: during cooling and heating. Next, Kim et al. [27] prepared Ti–Ni–Mo fibers by a melt overflow process, adjusting the molybdenum content (0.3 at.% to 0.5 at.%) to replace the content of nickel in the alloy. The research showed a phase transformation in two stages $B2-R-B19'$, and a reduction in the final austenite transformation temperature from 43 °C to –42 °C. More recently, Choe et al. [3] analyzed the impact of adding Mo (0.1 at.% to 0.5 at.%) on the surface characteristics of the Ni–Ti alloy used in dental devices. The authors concluded that the increase in Mo resulted in the emergence of the R-phase and a decrease in the temperature of the formation of the R-phase. Another significant finding was the reduction in the corrosion current density with the addition of Mo, suggesting the feasibility of applying the alloy in files for dental treatment, given its excellent resistance to corrosion and fatigue.

Given the above, there need to be more extensive studies on Ti–Ni–Mo alloys, and the lack of reports in the scientific literature on Ti–Ni–Mo alloys with percentages more significant than 2 at.% of Mo establish an evident lack of knowledge. Plasma arc melting is a method of manufacturing this alloy that allows for obtaining homogeneous alloys [28] with a low risk of contamination, and these factors are crucial to guarantee the accuracy and effectiveness of shape recovery. In addition, research relating corrosion resistance to the possible applications of these alloys is still scarce, reinforcing the need for additional studies in this field.

This study intends to fill in the existing gaps in the characterization of Ti–Ni–Mo alloys. Through the plasma arc melting process, the alloys will be manufactured, and nickel will be replaced by Mo, generating six different compositions, designated by $Ti_{50}Ni_{50-x}Mo_x$, where 'x' represents the proportions of Mo: 0, 0.5, 1, 2, 3, and 4 at.%. The methodological approach of this study focuses on the analysis of the influence of increasing Mo content on the microstructure, phase transformation temperatures, microhardness, and corrosion resistance.

2. Materials and Methods

2.1. Sample Fabrication

To obtain the compositions of the Ti–Ni–Mo alloys, the following metals were used: biomedical titanium (grade 2), electrolytic nickel (>99.98%), and Ti–Mo orthodontic wires purchased from Dental supplier Morelli® (Sorocaba-SP, Brazil). The masses were measured on an analytical balance to obtain ingots weighing approximately 30 g. Before starting the melting process, subjecting the different elements to chemical pickling is essential. In this work, the solution followed the ASTM B600-11R17 standard [29], consisting of 3 mL of hydrofluoric acid, 30 mL of nitric acid, and 67 mL of water.

For the manufacture of Ti–Ni–Mo bulk alloys, the plasma skull push-pull (PSP) melting method was used, using a plasma arc melting machine (model Discovery All Metals from EDG Equipamentos, São Carlos, SP, Brazil) in which the raw metals are melted and remelted 3 times in a copper crucible under argon gas atmosphere, at a pressure of 1.5 kgf/cm². Then, the remelted material is injected into a copper cylindrical mold, resulting in an ingot with dimensions of 30 mm in length and 10 mm in diameter. This technique was implemented by Araújo et al. [30] for the production of Ni–Ti alloys and Cu-based alloys. After obtaining the ingots, the samples were cut into discs 2 mm in thickness through electroerosion machining (EDM) in low-current discharges.

Table 1 summarizes the nominal chemical compositions of this study's Ti–Ni–Mo alloys. These compositions were chosen based on the literature review described in the introduction section. Since the literature presents alloys with up to 2 at.% of Mo, we decided to expand the analysis up to 4 at.% of Mo.

Table 1. Nominal atomic chemical composition of the alloys produced in this work.

Ni–Ti	Ti–Ni–Mo _{0.5}	Ti–Ni–Mo ₁	Ti–Ni–Mo ₂	Ti–Ni–Mo ₃	Ti–Ni–Mo ₄
Ti ₅₀ –Ni ₅₀	Ti ₅₀ –Ni _{49.5} – (0.5 at.% Mo)	Ti ₅₀ –Ni ₄₉ – (1 at.% Mo)	Ti ₅₀ –Ni ₄₈ – (2 at.% Mo)	Ti ₅₀ –Ni ₄₇ – (3 at.% Mo)	Ti ₅₀ –Ni ₄₆ – (4 at.% Mo)

2.2. Sample Preparation

After the cutting step, the disks obtained were sanded on a manual sander with silicon carbide (SiC) sandpaper, with grains: 220, 400, 600, 800, and 1200. Then, another polishing procedure was conducted with a manual polisher but using alumina 1 µm, 0.3 µm, and 0.05 µm. After manual polishing, the samples were submitted to an electrolytic polishing process, carried out in an electronic polisher ELECTROMET 4 from BUEHLER using a solution containing 910 mL of distilled water, 60 mL of 70% nitric acid, and 30 mL of 60% hydrofluoric acid. This solution follows the ASTM E 407–99 standard [31].

2.3. Alloy Characterization and Chemical Composition

Initially, the alloys were characterized in terms of morphology through scanning electron microscopy tests using a Tescan microscope, model Vega3 XM (Brno—Kohoutovice, Czech Republic). Next, chemical composition measurements were performed using an Oxford digital energy dispersive spectrometer (EDS). The samples were also characterized in terms of their microstructure through X-ray diffraction (XRD) tests using a Shimadzu diffractometer, model 6100 Shimadzu 6100, with Cu–K α ($\lambda = 1.5418 \text{ \AA}$) radiation, with conditions of 30 kV and 30 mA. XRD patterns were obtained in continuous mode in the 2θ region from 20 to 80° , with a step of 0.02° , speed of $2^\circ/\text{min}$, and angle of incidence of 7° . The COD (Crystallography Open Database) cataloging sheets of patterns were used to identify the phases. The thermal characterization was conducted from DSC tests using a calorimeter model Q20 from the manufacturer TA Instruments. The parameters used were: heating and cooling rate of $10 \text{ }^\circ\text{C}/\text{min}$ and temperature range from $100 \text{ }^\circ\text{C}$ to $-60 \text{ }^\circ\text{C}$. The phase transformation temperatures were determined by the tangent method, according to the ASTM F2004-05 [32], using the Universal Analysis 2000 software (TA Instruments). The microhardness test was carried out in a Dynamic Ultra Microhardness tester (DUH-211/DUH-211S, SHIMADZU) under room temperature around $25 \text{ }^\circ\text{C}$, with a Berkovitch indenter (Young Modulus: 1141 GPa, Poisson coefficient: 0.07). This equipment makes it possible to obtain the modulus of elasticity and microhardness.

2.4. Corrosion Analysis

The electrochemical measurements of corrosion were performed in a cell composed of three electrodes: a saturated calomel electrode (SCE) that was used as a reference electrode, a platinum electrode as an auxiliary, and the disks of the Ni–Ti and $\text{Ti}_{50}\text{Ni}_{50-x}\text{Mo}_x$ samples as a working electrode with 0.2728 cm^2 of exposed area.

A phosphate-buffered saline (PBS) solution, pH 7.4, which simulates human blood, was used as an electrolyte. Its elaboration followed the ASTM F2129-08 standard [33], and the concentrations of the reagents are shown in Table 2.

Table 2. Composition of the electrolyte solution used in the corrosion tests.

Reagents	NaCl	KCl	Na_2HPO_4	KH_2PO_4
Concentration (g/L)	8.0	0.2	1.15	0.2

The potentiodynamic polarization technique was used to determine the electrochemical parameters of corrosion: corrosion potential (E_{Corr}) and corrosion current density (I_{Corr}). The polarization curves were obtained with a sweep rate of $1 \text{ mV}/\text{s}$ through an Autolab PGSTAT302N potentiostat/galvanostat connected to a computer using the NOVA 2.1 software.

The calculation of the corrosion current was based on the Stern–Geary equation, which was also used in the work by [34] and is presented in Equation (1).

$$I_{\text{Corr}} = \frac{b_a \cdot b_c}{2.3(b_a + b_c)R_p} \quad (1)$$

where b_a and b_c represent the slopes of the anodic and cathodic Tafel lines, respectively, and I_{Corr} represents the corrosion current.

Electrochemical impedance spectroscopy (EIS) tests were performed with the equipment used for potentiodynamic polarization, with a frequency range of 100 kHz to 0.01 Hz and an amplitude of 0.01 V. EIS tests were measured at the open circuit potential (EOCP), obtained with 60 min of stabilization. The Nyquist diagrams were adjusted through an equivalent electrical circuit by NOVA 2.1.4.

3. Results and Discussion

3.1. X-ray Diffraction

The spectra obtained in the XRD analysis for the different compositions studied in the state as cast are shown in Figure 1. All peaks were identified by the HighScore Plus software (Version 5.1), adopting data from the COD base (Crystallography Open Database) as a reference. For the Ni–Ti binary alloy, the martensite and austenite phases were identified. The coexistence of the austenite and martensite phases in diffractograms was also observed by other authors [21,26,35]. The monoclinic martensite phase (B19') was identified by comparing with the chart (2107170) in the planes (002), (−111), (020), (012), (022) and with chart (9015733) in the plane (011). The B2 austenite phase was identified by comparing with the chart (1100132) in the planes (010), (011), (020), and (121).

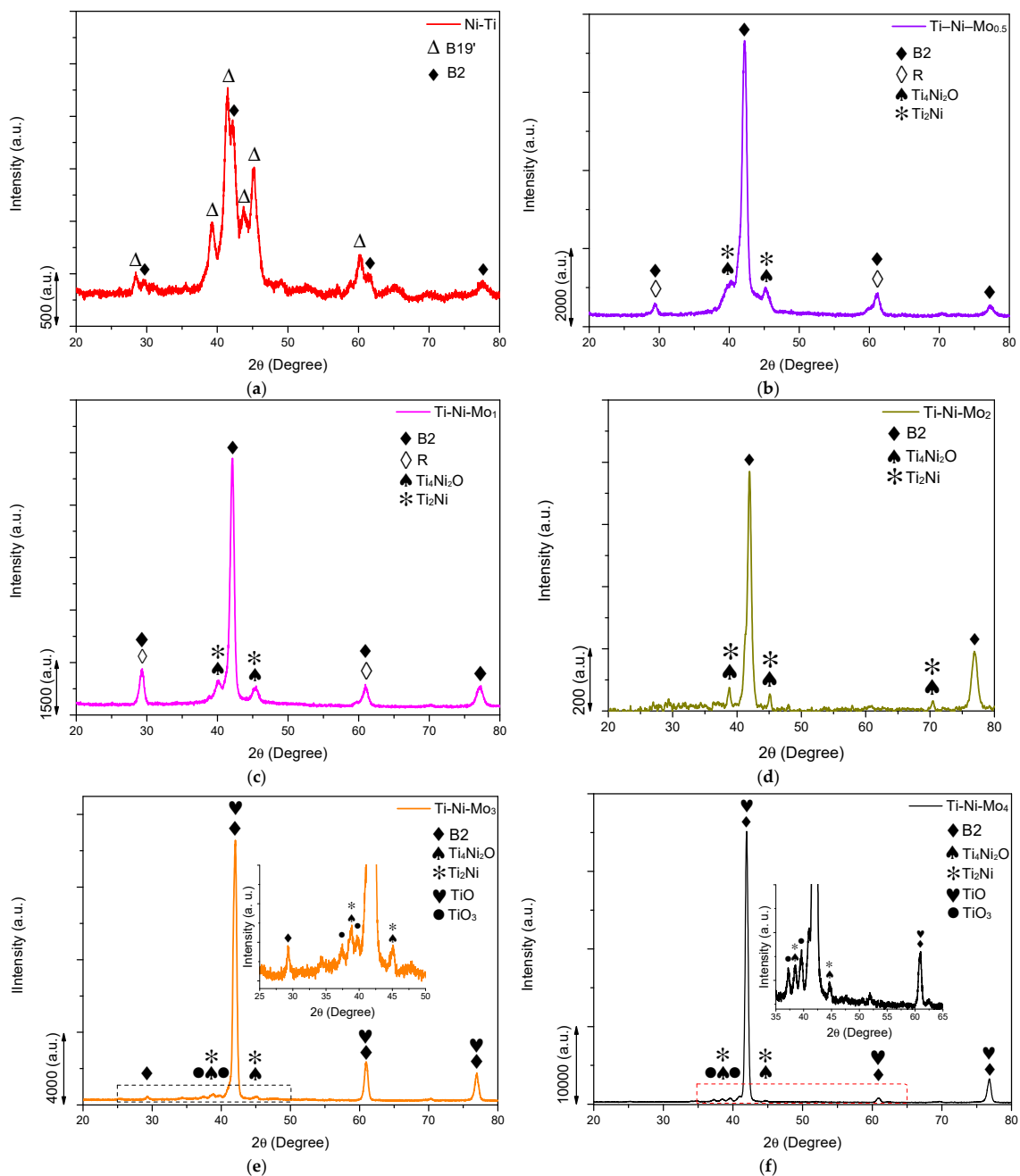


Figure 1. X-ray diffractograms of the alloys: (a) Ni–Ti, (b) Ti–Ni–Mo_{0.5}, (c) Ti–Ni–Mo₁, (d) Ti–Ni–Mo₂, (e) Ti–Ni–Mo₃, and (f) Ti–Ni–Mo₄, as cast, obtained at room temperature.

Still, Figure 1 shows that the increase in the molybdenum content caused a change in the oxides formed on the surface of the samples. Some oxides were identified in the samples from the content of 3 at.% of molybdenum. The formation of oxides occurs due to the high reactivity of these elements with oxygen, as also seen by Hsieh et al. [42]. Ti–Ni–Mo₃ and Ti–Ni–Mo₄ samples showed TiO oxides (planes (020), (022), and (222) of chart 1536851) and TiO₃ (planes (004) and (112) of chart 1529954). The presence of these oxides was also reported by Swain et al. [43] and Odetola et al. [44]. This behavior can be explained by the increase in the Ti/Ni ratio, as, according to Chan et al. [45], the increase in the Ti/Ni ratio favors the increase in TiO and TiO₂ oxides.

3.2. Scanning Electron Microscopy and Chemical Composition

In manufacturing, molybdenum was added in different atomic percentages in substitution to compare the Ni content in the Ni–Ti alloy. Molybdenum is a β -stabilizer, and the variation in its atomic percentage in the alloy can cause different microstructures and properties to be obtained [46].

According to Xu et al. [47], due to their intermetallic nature, the microstructures and properties of binary Ni–Ti alloys are very sensitive to the ratio of Ni and Ti contents. Therefore, deviations in stoichiometry, such as adding elements to form ternary systems or replacing Ti or Ni, can cause the precipitation of secondary phases—during solidification or heat treatment at high temperatures, for example.

After fabrication, the Ni–Ti, Ti–Ni–Mo_{0.5}, Ti–Ni–Mo₁, Ti–Ni–Mo₂, Ti–Ni–Mo₃, and Ti–Ni–Mo₄ alloys were characterized according to their morphology. For this, the scanning electron microscopy (SEM) technique was used to identify the chemical composition by EDS. The images referring to the alloys obtained in the state as cast (post-melting without heat treatment) are shown in Figure 2.

According to the image presented in Figure 2a, it is possible to observe that the Ni–Ti sample presents a uniform microstructure with well-defined grain boundaries. In addition, evidence of the martensite phase (B19') was observed, indicating that this Ni–Ti sample presents the martensite phase at room temperature. A similar behavior was observed by Marattukalam et al. [48], in which the processed Ni–Ti alloy clearly showed well-defined grain boundaries and the wrinkled appearance of the martensite phase.

As the Ni–Ti sample presented a homogeneous microstructure, that is, the presence of precipitates and intermetallic compounds was not observed, the chemical composition measurement through EDS was carried out over the entire region shown in Figure 2a, and the result is available in Table 3. The data indicate that the Ni–Ti sample is rich in titanium and differs by 2% from the expected one since the nominal composition was an equiatomic alloy. This variation in composition may occur due to the volatilization of nickel, the most volatile element in the alloy. According to Gale, William and Totemeier [49], nickel has a higher evaporation rate than titanium.

The image with 2000 \times magnification of the sample with 0.5 at.% molybdenum is shown in Figure 2b. It is observed that this sample exhibits well-defined grain boundaries and diverse intragranular structures. It is also possible to verify some equiaxed grains observed in the Ni–Ti alloy, as well as the presence of precipitates and the wrinkled appearance characteristic of the martensite phase (B19'). The precipitates observed in the Ti–Ni–Mo_{0.5} sample were analyzed using the EDS test, and, according to the chemical composition shown in Table 3, it can be seen that they are precipitates of Ti₂Ni and oxides of Ti₄Ni₂O. A similar composition was reported by Klopotov et al. [50].

Figure 2c shows the image referring to the Ti–Ni–Mo₁ sample at 2000 \times magnification. As shown in the image, this sample exhibits a markedly different microstructure from the binary alloy. It is a characteristic hypo eutectic microstructure, composed of a matrix phase, which is observed in the micrographs as the region with a light gray color, surrounded by an interdendritic eutectic structure, identified as the darkest region. The two identified regions were analyzed by EDS and are presented in Table 3. The data indicate that the dark

region (interdendritic eutectic structure) presents molybdenum content below the expected (0.6 at.%), while the light region presents the expected composition (1.1 at.%).

Figure 2d confirms that the Ti–Ni–Mo₂ alloy presents structures with areas of dendritic crystallization and coarse precipitates of Ti₂Ni. In addition, fine precipitates of TiNi crystallized separately in the matrix, and Ti₄Ni₂O precipitated in a rounded and segregated form. These precipitates were identified through EDS analysis; the data are shown in Table 3. In the work of Klopotov et al. [50], the effect of adding Molybdenum (0.3 at.%) and Vanadium (2 at.%) in the Ni–Ti binary alloy was evaluated, and the results revealed the presence of precipitates similar to those identified in this work for the Ti–Ni–Mo₂ alloy.

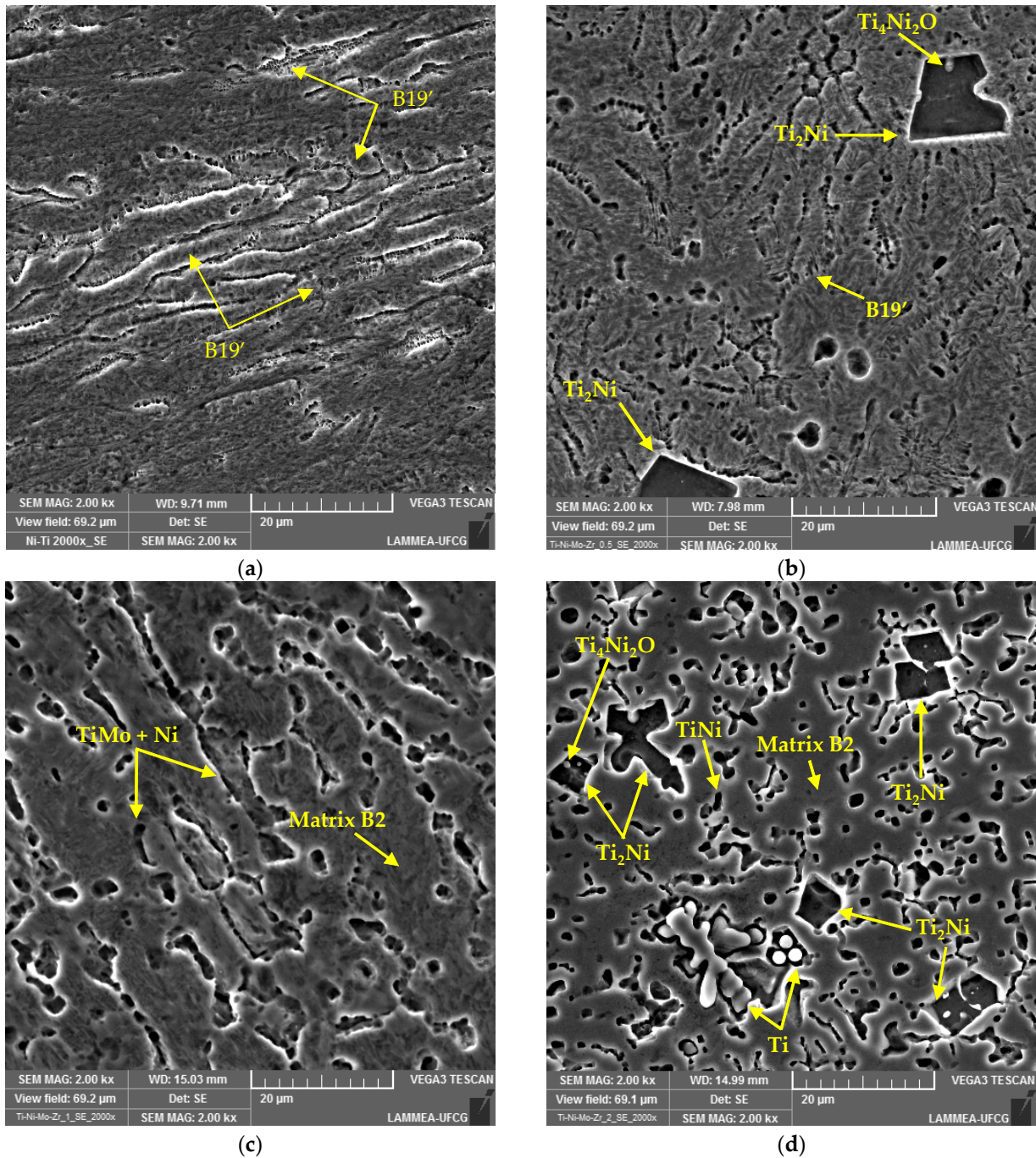


Figure 2. Cont.

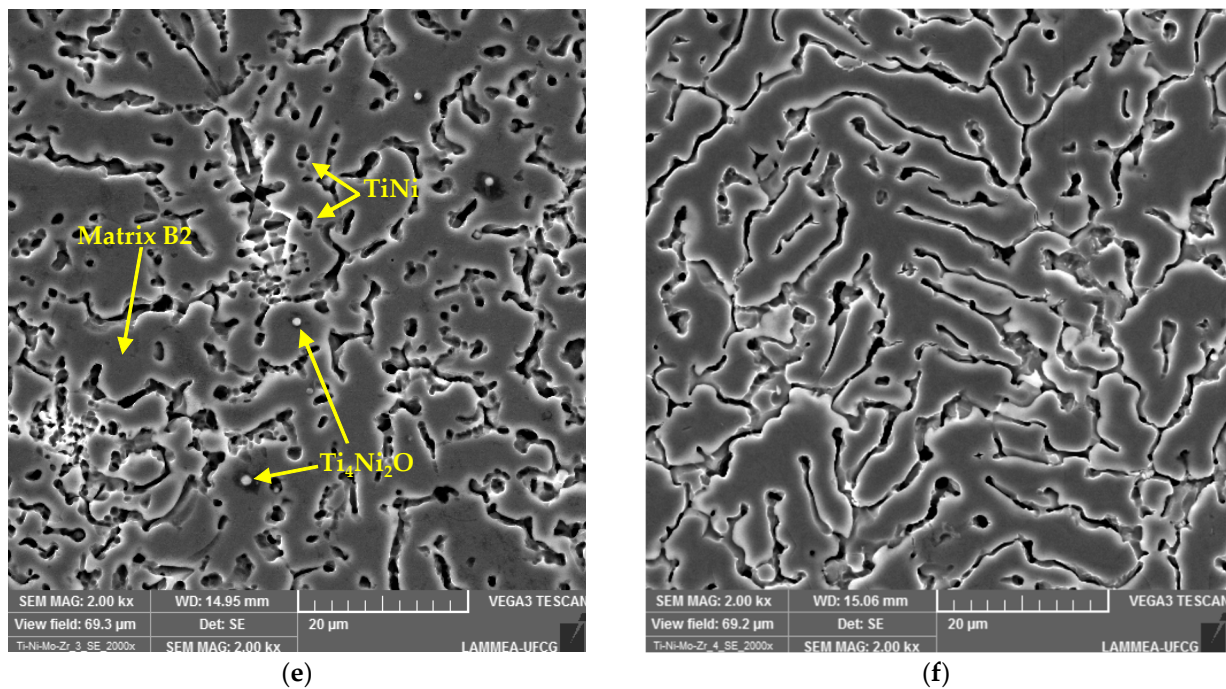


Figure 2. SEM images of the alloys: (a) Ni–Ti, (b) Ti–Ni–Mo_{0.5}, (c) Ti–Ni–Mo₁, (d) Ti–Ni–Mo₂, (e) Ti–Ni–Mo₃, and (f) Ti–Ni–Mo₄ (magnification of 2000×).

Table 3. Quantitative data of the chemical composition of the phases found in the alloys: Ni–Ti, Ti–Ni–Mo_{0.5}, Ti–Ni–Mo₁, Ti–Ni–Mo₂, Ti–Ni–Mo₃, and Ti–Ni–Mo₄.

Alloys	Phases	Ti (at.%)	Ni (at.%)	Mo (at.%)	O (at.%)
Ni–Ti	B19'	52.3 ± 0.1	47.7 ± 0.1	-	-
Ti–Ni–Mo _{0.5}	Ti ₂ Ni (Mo)	67.7 ± 0.03	32.1 ± 0.02	0.2 ± 0.01	-
	Ti ₄ Ni ₂ O (Mo)	47.0 ± 0.3	33.5 ± 1.9	2.0 ± 0.4	17.5 ± 1.2
	B19'-Matrix	52.0 ± 0.12	47.4 ± 0.1	0.55 ± 0.01	-
Ti–Ni–Mo ₁	TiMo + Ni	51.5 ± 0.5	47.9 ± 0.5	0.6 ± 0.1	-
	B2-Matrix	51.7 ± 0.05	47.1 ± 0.03	1.1 ± 0.01	-
Ti–Ni–Mo ₂	Ti	94.2 ± 4	5.7 ± 4	-	-
	TiNi	51.2 ± 0.8	48.7 ± 0.8	-	-
	Ti ₂ Ni (Mo)	62.7 ± 0.2	36.3 ± 0.2	1.04 ± 0.02	-
	Ti ₄ Ni ₂ O (Mo)	47 ± 0.3	33.5 ± 1.9	2.0 ± 0.4	17.5 ± 1.2
	B2-Matrix	51.1 ± 0.3	46.7 ± 0.3	2.2 ± 0.04	-
Ti–Ni–Mo ₃	TiNi	52.4 ± 0.3	47.6 ± 0.3	-	-
	Ti ₄ Ni ₂ O (Mo)	47 ± 0.3	33.5 ± 1.9	2.0 ± 0.4	17.5 ± 1.2
	B2-Matrix	50.3 ± 0.8	46.2 ± 0.8	3.4 ± 0.03	-
Ti–Ni–Mo ₄	B2-Matrix	50.1 ± 0.2	45.5 ± 0.3	4.3 ± 0.2	-

The images presented in Figures 1f and 2e represent the Ti–Ni–Mo₃ and Ti–Ni–Mo₄ alloys, respectively, and show structures with areas of dendritic crystallization not showing characteristics of the martensite phase. It can be seen that these alloys have two regions, one light and one dark. A similar result was found by Chen et al. [51] when evaluating the microstructure of a Ti–Ni–Nb alloy with the addition of molybdenum. The image shown in Figure 2e shows that the Ti–Ni–Mo₃ alloy has structures with areas of dendritic crystallization and some precipitates that were identified by EDS as TiNi precipitates and Ti₄Ni₂O-type oxides, without evidence of the characteristic wrinkled appearance of the martensite phase. In Figure 2f, the presence of precipitates and intermetallic compounds

was not observed, and thus, the measurement of chemical composition through EDS was then carried out over the entire region shown in Figure 2f.

The data presented show that the Ti–Ni–Mo_{0.5}, Ti–Ni–Mo₁, Ti–Ni–Mo₂, and Ti–Ni–Mo₃ alloys presented different phases, such as precipitates and oxides; this result corroborates what was found in the XRD diffractograms. Among those cited, the alloy with 2 at.% of molybdenum presented more precipitates, while the Ni–Ti and Ti–Ni–Mo₄ alloys did not. Concerning the matrix phase of each alloy, it was observed that the percentages of molybdenum obtained confirmed what was expected, indicating that the plasma arc melting process was able to produce Ti–Ni–Mo alloys with compositional homogeneity.

It is essential to highlight that the EDS analysis, although applicable to identifying the elements present in the sample, has limitations. In particular, the interaction volume in EDS analysis can include surrounding areas, which can result in an inaccurate representation of the chemical composition of an individual phase or area. Furthermore, EDS analysis is a semi-quantitative method subject to measurement errors. Thus, although the EDS data provide us with valuable information about the overall chemical composition of our samples, the data must be interpreted with care when it comes to determining the chemical composition of individual phases, and it is necessary to confirm with XRD data.

3.3. Transformation Temperatures

The thermal study of the samples was possible thanks to the DSC tests, and the curves resulting from the tests are shown in Figure 3, from which the thermally induced transformation behavior of the evaluated samples can be observed. The exothermic peak on cooling represents the transformation from austenite to martensite, and the endothermic peak on heating is related to the reverse transformation from martensite to austenite.

It is verified that the thermogram of the binary alloy is altered with the addition of Mo, and the variation of the Mo content in the ternary alloys also causes alterations in the transformation temperatures. The evaluation of the results presented allows establishing a direct relationship between the variation in the composition of the alloys with the manifested thermal behavior; therefore, the increase in the molybdenum content causes a decrease in the temperature R_s . Similar behavior was observed by Jiang et al. [52]. These researchers found that the peaks of the martensite transformation and the R-phase transformations' peaks gradually shifted to lower temperatures with increasing Mo content. Based on this assumption, we can say that the corresponding curves of the Ti–Ni–Mo₂, Ti–Ni–Mo₃, and Ti–Ni–Mo₄ alloys did not show phase transformation peaks in the range analyzed here because the increase in molybdenum content caused a significant shift to lower temperatures.

From these, DSC curves were extracted: The start and end temperatures of the R-phase, R_s and R_f ; the start and end temperatures of the martensite transformation, M_s and M_f ; and the start and end temperatures of the reverse transformation, A_s and A_f , as well as the enthalpies of transformation of the R-phase (ΔH_R), of the martensite phase (ΔH_M) on cooling and of the austenite phase (ΔH_A) on heating. These values were determined from the intersections of the tangents for the cooling and heating peaks by taking the inflection points and are shown in Table 4.

Table 4. Phase transformation temperatures and phase transformation enthalpies obtained from the DSC curves.

Samples	R_s (°C)	R_f (°C)	M_s (°C)	M_f (°C)	A_s (°C)	A_f (°C)	ΔH_R (J/g)	ΔH_M (J/g)	ΔH_A (J/g)
Ni–Ti	-	-	35.1	11.8	41.7	70.9	-	26.2	27.2
Ti–Ni–Mo _{0.5}	22.2	−5.6	−10.9	−37.7	8.8	40.5	2.9	6.2	18.9
Ti–Ni–Mo ₁	12.4	−11.7	−20.9	-	−21.7	23.9	3.7	-	15.2

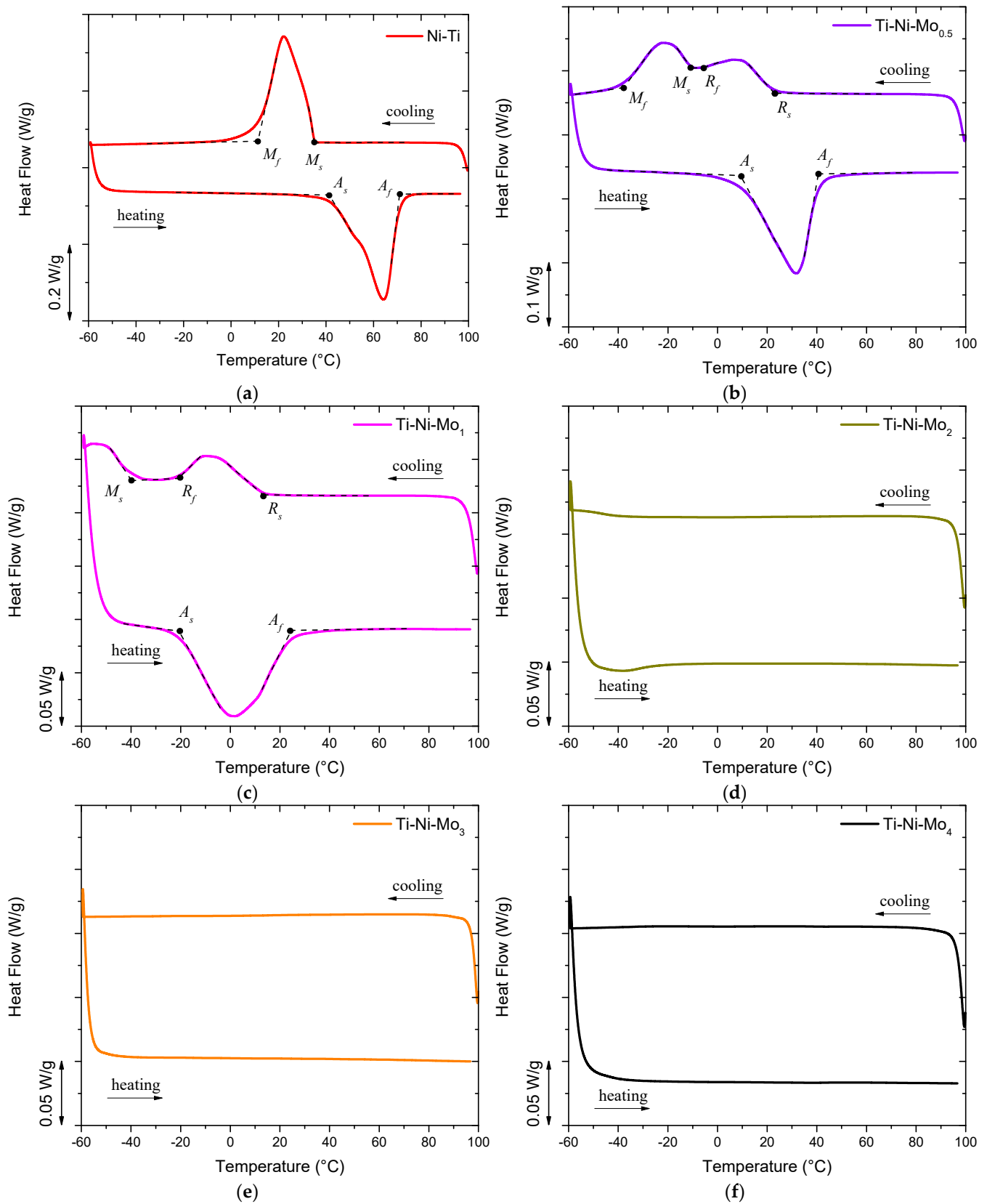


Figure 3. DSC curves of the alloys as cast: (a) Ni-Ti, (b) Ti-Ni-Mo_{0.5}, (c) Ti-Ni-Mo₁, (d) Ti-Ni-Mo₂, (e) Ti-Ni-Mo₃, and (f) Ti-Ni-Mo₄.

The data in Table 4 confirm what was observed—the addition of molybdenum to the Ni–Ti alloy caused the decoupling of the R-phase, and the increase in the molybdenum content in the alloy caused a displacement in the phase transformation peaks to lower temperatures. A variation of 9.8 °C was observed for the beginning of the R-phase transformation and 30.5 °C for the beginning of the austenite transformation, a variation caused by an increase of 0.5% in the molybdenum nominal composition.

3.4. Microhardness and Modulus of Elasticity

The instrumented indentation technique measures the yield strength of the material. It can also be used to measure mechanical properties of materials, such as hardness and modulus of elasticity. Some works in the literature [28,53–55] report using this technique to determine the hardness and modulus of elasticity of materials based on Ni–Ti.

Table 5 presents data on microhardness and modulus of elasticity for alloys with different percentages of molybdenum. The data in Table 5 indicate that the increase in the molybdenum content causes a decrease in the hardness and modulus of elasticity. Similar behavior was observed by Ozaki et al. [56], when adding a beta-stabilizing element to the titanium alloy. In another paper, Zhao et al. [57] describe the characterization of a Ni–Ti alloy with niobium addition. These authors verified that the addition of niobium caused a decrease in the values of microhardness and modulus of elasticity and that this softening behavior would be attributed to the effect of damage, which is caused by the implanted ions that transfer enough energy to target atoms during a series of collisions and manages to displace them from their network location. Our hypothesis is that the same phenomenon occurs in alloys based on Ni–Ti with the addition of Mo.

Table 5. Microhardness and modulus of elasticity of the alloys as cast: Ni–Ti, Ti–Ni–Mo_{0.5}, Ti–Ni–Mo₁, Ti–Ni–Mo₂, Ti–Ni–Mo₃, and Ti–Ni–Mo₄.

Alloy	Microhardness (HV)	Modulus of Elasticity (GPa)
Ni–Ti	494 ± 12	71 ± 5
Ti–Ni–Mo _{0.5}	461 ± 29	74 ± 5
Ti–Ni–Mo ₁	222 ± 18	52 ± 2
Ti–Ni–Mo ₂	339 ± 24	65 ± 3
Ti–Ni–Mo ₃	294 ± 39	65 ± 7
Ti–Ni–Mo ₄	272 ± 17	63 ± 5

It is essential to point out that the samples with higher molybdenum contents showed a modulus of elasticity around 63 GPa, which is interesting for applications such as biomaterials since the titanium used for this purpose has a high modulus of elasticity (111 GPa), and this causes discomfort to the patient. Furthermore, it can cause the phenomenon known as stress shielding due to the rigidity mismatch between the bone and the implant [58]. According to Figure 4, we observe that the modulus of elasticity of dense human bone is around 26 GPa and that the value found in this work (63.8 ± 7.8 GPa) is closer to the desired one when compared to commercially pure titanium (CpTi).

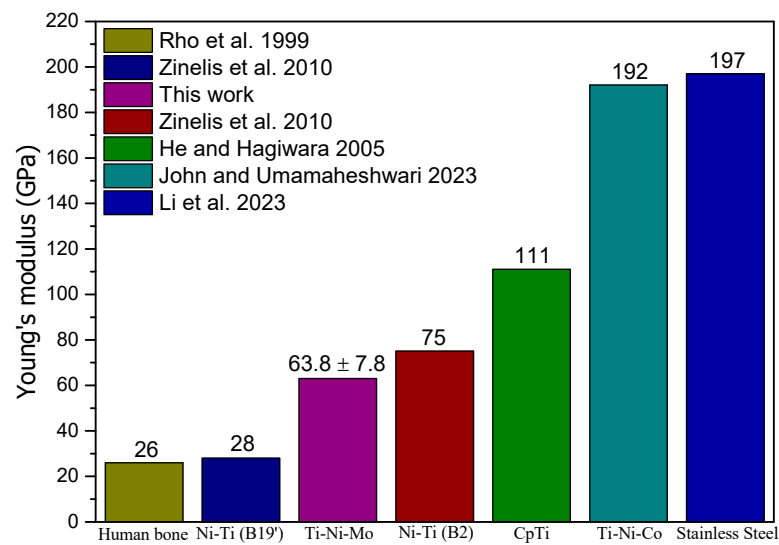


Figure 4. Values of modulus of elasticity of metallic materials used as biomaterials [59–63].

3.5. Corrosion Resistance Evaluation

Figure 5 presents the curves representing the variation of the open circuit potential (E_{OCP}) measured before the potentiodynamic polarization tests for each of the samples of the studied alloys immersed in a PBS solution for 3600 s. It is noticed that after the immersion of the working electrodes, the potentials are displaced in the direction of more positive potentials, tending to a stabilization. According to Oliveira et al. [64], this behavior is characteristic of metals that present spontaneous formation of a passive film on the metallic surface, that is, that undergo passivation, being able to control and reduce the dissolution of the alloy. Saebnoori et al. [65] clarify that, during immersion in an electrolyte, dissolved oxygen ions adsorb on the surface of the electrode and react with ions of the metallic alloy to form an oxide layer, which inhibits the conductivity of ions at the electrode/electrolyte interface, so, forming a protective film. As a result, there is a decrease in the anodic dissolution current, as indicated by the increase in E_{OCP} , reaching a stable condition after the completion of passive film formation.

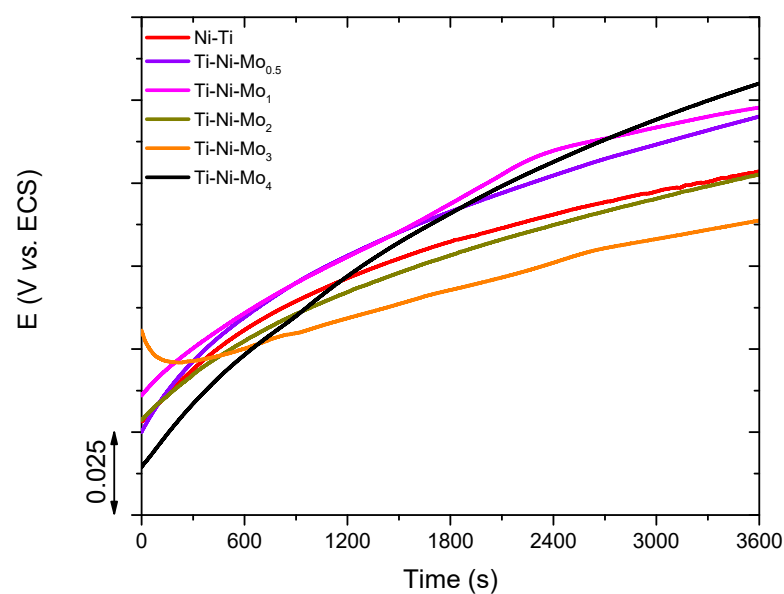


Figure 5. Curves of Open Circuit Potential of Ni-Ti, Ti-Ni-Mo_{0.5}, Ti-Ni-Mo₁, Ti-Ni-Mo₂, Ti-Ni-Mo₃, and Ti-Ni-Mo₄, obtained in SBF at room temperature.

The curves presented in Figure 5 also reveal that the E_{OCP} values observed at the end of the measurements do not vary uniformly with the variation in the composition of the alloys. Therefore, it is not possible to propose that there is a tendency in its behavior related to the Mo content. Unlike what was observed by Li et al. [66], who, when analyzing Ni–Ti–Nb thin films deposited by cathodic sputtering (sputtering) on silicon substrates (Si) and annealed at 600 °C for crystallization, found that in a 3.5% NaCl solution at 25 °C, a general trend can be obtained, so that the open-circuit potentials of the films increase as the Nb content increases, even presenting higher values compared to the Ni–Ti film. The authors point out that the increase in E_{OCP} toward more positive values indicates the formation of a thicker and chemically more stable passivation layer, while the decay of the potential toward more negative values indicates the dissolution of the passive layer. On the other hand, the results of potentiodynamic polarization and electrochemical impedance must be considered to arrive at a concrete result.

Figure 6 shows the polarization curves, from which the corrosion potential (E_{Corr}), corrosion current (I_{Corr}), and polarization resistance (R_p) values were extracted, which are shown in Table 6.

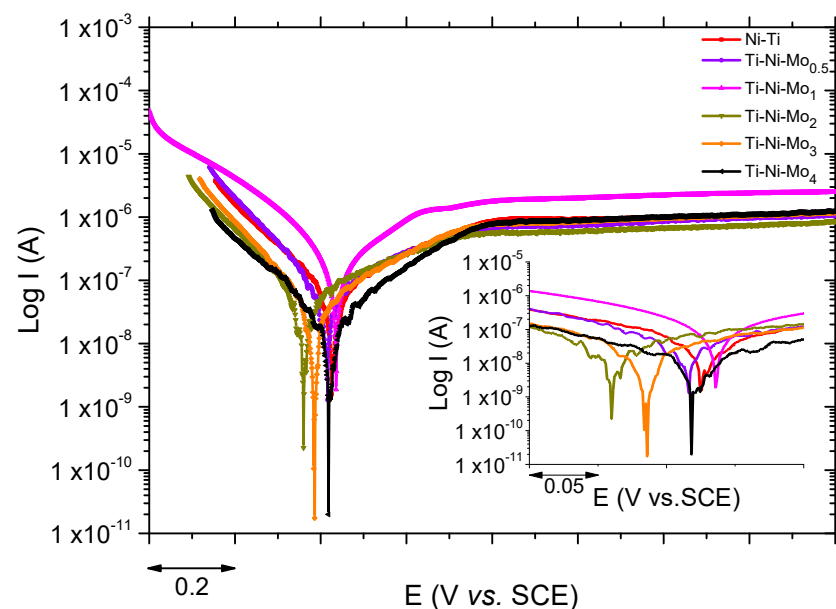


Figure 6. Potentiodynamic polarization curves of Ni–Ti, Ti–Ni–Mo_{0.5}, Ti–Ni–Mo₁, Ti–Ni–Mo₂, Ti–Ni–Mo₃, and Ti–Ni–Mo₄ obtained in SBF at room temperature.

Table 6. Electrochemical parameters obtained from the potentiodynamic polarization curves.

Alloy	E_{OCP} (V)	E_{Corr} (V)	I_{Corr} (μ A)	ba (V/dec)	bc (V/dec)
Ni–Ti	−0.346	−0.377	32.2	0.364	0.182
Ti–Ni–Mo _{0.5}	−0.330	−0.384	27.0	0.330	0.152
Ti–Ni–Mo ₁	−0.327	−0.363	23.9	0.172	0.281
Ti–Ni–Mo ₂	−0.347	−0.440	22.5	0.392	0.156
Ti–Ni–Mo ₃	−0.361	−0.420	16.9	0.298	0.143
Ti–Ni–Mo ₄	−0.320	−0.378	11.3	0.246	0.196

Figure 6 and Table 6 show that the addition of molybdenum to the Ni–Ti alloy caused an increase in corrosion resistance. It is observed that the samples presented the phenomenon of formation of the passivation film characterized by the stability of the current in the range of 0 to 0.8 V. As can be seen in the image, the corrosion potentials (E_{Corr}) were very close and, therefore, due to dealing with a thermodynamic parameter that only indicates a trend, it is advisable to evaluate the I_{Corr} parameter to quantify the corrosive behavior of these alloys better. According to the data in Table 6, all samples show a small

I_{Corr} (μA level), proving the passive layer's effective protection. The Ti–Ni–Mo samples have lower I_{Corr} values than the Ni–Ti sample, which suggests that Mo additions positively influenced the corrosion resistance of these alloys.

The corrosive behavior observed in the polarization tests was similar to that observed in the OCP curves, so the results did not vary uniformly with the increase in molybdenum content. However, alloys with higher molybdenum contents showed better corrosion resistance. This behavior can be explained by TiO and TiO₃ oxides detected through XRD only for Ti–Ni–Mo₃ and Ti–Ni–Mo₄ samples. Mareci et al. [67] evaluated the electrochemical behavior of titanium alloys containing molybdenum and tantalum and found an improvement in the corrosion resistance of these alloys when compared to titanium used for implants CpTi. The authors attributed this improvement in resistance to the presence of TiO₂. In another work, Zhou and Luo [68] carried out a comparative study between Ti–Mo and CpTi alloys and found that CpTi showed good corrosion behavior due to the formation of a protective film of TiO₂ oxide and Ti–Mo alloys showed good corrosion behavior due to the passive film formation of a mixture of TiO₂ and MoO₃. The authors pointed out that Ti–Mo alloys exhibited better corrosion resistance than CpTi, suggesting that the passive film of a mixture of TiO₂ and MoO₃ is more stable and stronger than the passive TiO₂ film, and that Ti–Mo is more suitable than CpTi for biomedical application from the point of view of good corrosion resistance.

In order to compare the oxide film formed on the surface of the samples when immersed in PBS, electrochemical impedance spectroscopy tests were carried out, and the results are presented in the form of a Nyquist diagram in Figure 7. All impedance spectra showed a capacitive double layer (CPE) behavior characterized by an unfinished semicircle. This behavior is typical of passive materials, involving a protective film with high corrosion resistance. The shapes of the curves are very similar, indicating no changes in the corrosion mechanism of any sample [69]. However, with the increase in the Mo content in the alloy, an increase in the diameter of the curves is observed. The larger the diameter of this semicircle, the greater the material impedance, which translates into lower kinetics on the surface of the working electrode, making it difficult to transfer negatively charged species, according to Wu and He [70].

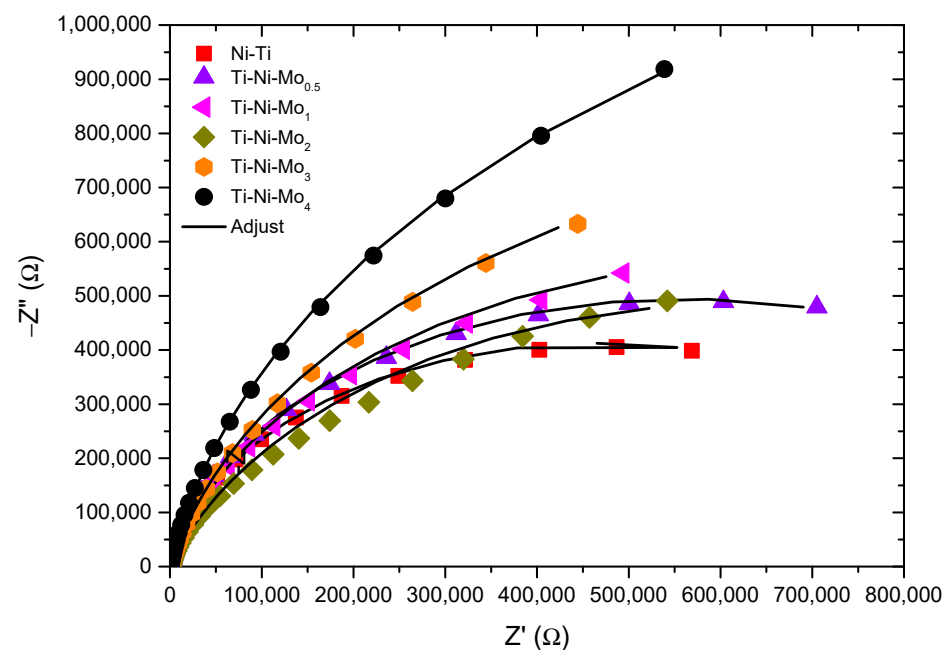


Figure 7. Nyquist diagrams for Ni–Ti, Ti–Ni–Mo_{0.5}, Ti–Ni–Mo₁, Ti–Ni–Mo₂, Ti–Ni–Mo₃, and Ti–Ni–Mo₄ obtained at open circuit potential.

The experimental data of the curves of the Nyquist diagram shown in Figure 7 were fitted through the equivalent electrical circuit, known as the Randles circuit, shown in Figure 8. The same circuit was used by Liu et al. [71] to fit spectra similar to those of this study. In this circuit, R_s is the solution resistance, R_p is the bias resistance (also known as the charge transfer resistance), and CPE is the capacitive double layer. The values of the parameters R_s , CPE, and R_p obtained from the equivalent electrical circuit are shown in Table 7.

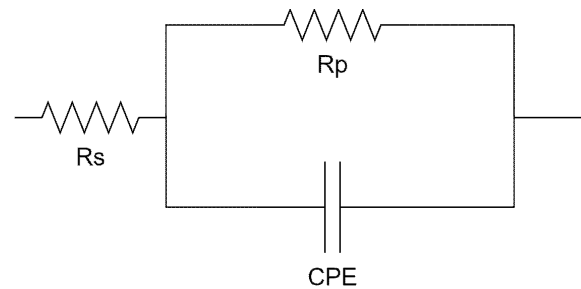


Figure 8. Equivalent electric circuit model to adjust the electrochemical impedance data.

Table 7. Adjustment parameters of the equivalent circuit of Ni–Ti, Ti–Ni–Mo_{0.5}, Ti–Ni–Mo₁, Ti–Ni–Mo₂, Ti–Ni–Mo₃, and Ti–Ni–Mo₄.

Liga	R_s ($\Omega \cdot \text{cm}^2$)	CPE ($\mu\text{F} \cdot \text{cm}^{-2}$)	n	R_p ($\text{K}\Omega \cdot \text{cm}^2$)
Ni–Ti	212	4.09	0.92	936
Ti–Ni–Mo _{0.5}	237	3.20	0.92	1120
Ti–Ni–Mo ₁	206	2.69	0.88	1370
Ti–Ni–Mo ₂	289	0.97	0.83	1280
Ti–Ni–Mo ₃	212	2.81	0.88	1880
Ti–Ni–Mo ₄	217	3.69	0.91	2710

The data in Table 7 quantify the Nyquist diagrams and confirm the behavior observed in the polarization curves. The alloy that showed the highest resistance to polarization, and consequently, the highest corrosion resistance, was the Ti–Ni–Mo₄ alloy.

4. Conclusions

Through the experimental study carried out in this work, it was possible to verify that:

- The addition of Mo in the Ni–Ti binary alloy and the changes in the Mo content in the ternary alloys caused changes in the microstructure, with the formation of different phases, precipitates (TiNi, Ti₂Ni), and oxides (Ti₄Ni₂O, TiO, and TiO₃).
- XRD analysis revealed an increase in the stability of the B2 phase when comparing Ni–Ti and Ti–Ni–Mo_{0.5} alloys. In this analysis, the monoclinic martensite phase (B19') was identified only for the Ni–Ti sample without molybdenum, suggesting that the change in the chemical composition of the alloy changed its microstructure to the austenite phase (B2).
- The thermal analysis carried out by DSC tests indicated that adding molybdenum in the Ni–Ti alloy caused the appearance of the R-phase, and the increase in the molybdenum content in the alloy caused a shift of the phase transformation peaks to lower temperatures.
- The results referring to microhardness and modulus of elasticity showed that the increase in molybdenum content tended to decrease the hardness and modulus of elasticity.
- Corrosion analysis revealed passivation film formation in all samples, giving these alloys high resistance to corrosion. In addition, it was verified that adding molybdenum to the Ni–Ti alloy increased corrosion resistance.

Finally, it is concluded that molybdenum is a β -stabilizer and its addition to the Ni–Ti alloy, as well as the increase in its content in the ternary alloy, caused changes in the microstructure that enabled the decrease in hardness, decrease in modulus of elasticity, and increased resistance to corrosion, and these results suggest that the ternary alloys obtained in this work can increase the field of application of Ni–Ti alloys, including in the field of biomaterials.

5. Patents

Josiane Dantas Costa has the patent BR102019014356A2 issued to the Federal University of Campina Grande.

Author Contributions: Conceptualization, J.D.C., R.A.C.S., C.J.A. and J.J.N.A.; methodology, J.D.C., M.B.S., A.F.A. and J.A.M.O.; investigation, J.D.C., M.B.S. A.F.A., J.A.M.O. and P.C.S.S.; literature search, M.B.S. A.F.A., J.A.M.O. and P.C.S.S.; data collection, J.D.C.; data analysis, R.A.C.S. and P.C.S.S.; figures, P.C.S.S.; study design, C.J.A. and R.A.C.S.; writing—original draft preparation, J.D.C.; writing—review and editing, M.B.S., A.F.A., J.A.M.O., J.J.N.A., A.R.N.C., C.J.A., J.M.P.Q.D. and A.G.B.L.; visualization, A.R.N.C., J.J.N.A., J.M.P.Q.D. and A.G.B.L.; supervision, R.A.C.S. and J.J.N.A.; project administration, R.A.C.S.; data interpretation, A.R.N.C., J.M.P.Q.D. and A.G.B.L.; funding acquisition, A.G.B.L., A.R.N.C., C.J.A. and J.M.P.Q.D. All authors have read and agreed to the published version of the manuscript.

Funding: This research was funded by the Brazilian National Council for Scientific and Technological Development (CNPq) for scholarship PQ-1C, grant number 302740/2018-0, and for the scholarship PQ-DT Level 2, grant number 308251/2020-2; the Paraíba State Research Support Foundation (FAPESQ-PB) for the project NISMArt, grant number 044/2023; and the Brazilian Coordination for the Improvement of Higher Education Personnel (CAPES) for the doctoral scholarship to Paulo César Sales da Silva and for the post-doctoral scholarship to Josiane Dantas Costa. In addition, this work is a result of the project “BlueWoodenHouse”, with the reference POCI-01-0247-FEDER-047157, co-funded by the European Regional Development Fund (ERDF) through the Operational Programme for Competitiveness and Internationalization (COMPETE 2020), under the Portugal 2020 Partnership Agreement, and the project “BlueHouseSim”, with reference 2022.06841.PTDC, funded by national funds (PIDDAC) through FCT/MCTES. Furthermore, this work was financially supported by Base Funding-UIDB/04708/2020 and Programmatic Funding-UIDP/04708/2020 of the CONSTRUCT-Instituto de I&D em Estruturas e Construções-funded by national funds through the FCT/MCTES (PIDDAC); and by FCT—Fundação para a Ciência e a Tecnologia through the individual Scientific Employment Stimulus 2020.00828.CEECIND.

Data Availability Statement: No new data were created or analyzed in this study. Data sharing is not applicable to this article.

Acknowledgments: We are grateful to the Laboratory of Microscopy of the Department of Mechanical Engineering (Federal University of Campina Grande) for technical support.

Conflicts of Interest: The authors declare no conflict of interest.

References

1. Frost, M.; Jury, A.; Heller, L.; Sedláč, P. Experimentally Validated Constitutive Model for NiTi-Based Shape Memory Alloys Featuring Intermediate R-Phase Transformation: A Case Study of Ni₄₈Ti₄₉Fe₃. *Mater. Des.* **2021**, *203*, 109593. [[CrossRef](#)]
2. Haskins, J.B.; Malmir, H.; Honrao, S.J.; Sandoval, L.A.; Lawson, J.W. Low-Temperature Mechanical Instabilities Govern High-Temperature Thermodynamics in the Austenite Phase of Shape Memory Alloy Constituents: Ab Initio Simulations of NiTi, NiZr, NiHf, PdTi, and PtTi. *Acta Mater.* **2021**, *212*, 116872. [[CrossRef](#)]
3. Choe, H.C.; Kim, J.U.; Park, S.K. Effects of Mo Content on Surface Characteristics of Dental Ni-Ti Alloys. *Corros. Sci. Technol.* **2023**, *22*, 64–72. [[CrossRef](#)]
4. Kumar, P.; Waghmare, U.V. First-Principles Phonon-Based Model and Theory of Martensitic Phase Transformation in NiTi Shape Memory Alloy. *Materialia* **2020**, *9*, 100602. [[CrossRef](#)]
5. Silva, P.C.S.; Grassi, E.N.D.; Araújo, C.J.; Delgado, J.M.P.Q.; Lima, A.G.B. NiTi SMA Superelastic Micro Cables: Thermomechanical Behavior and Fatigue Life under Dynamic Loadings. *Sensors* **2022**, *22*, 8045. [[CrossRef](#)]
6. Alshannag, M.J.; Alqarni, A.S.; Higazey, M.M. Superelastic Nickel–Titanium (NiTi)-Based Smart Alloys for Enhancing the Performance of Concrete Structures. *Materials* **2023**, *16*, 4333. [[CrossRef](#)]

7. Montenegro, E.O.S.; Grassi, E.N.D.; Simões, J.B.; Sales da Silva, P.C.; de Araújo, C.J. NiTi Shape Memory Alloy Cellular Meshes: Manufacturing by Investment Casting and Characterization. *Smart Mater. Struct.* **2020**, *29*, 125008. [[CrossRef](#)]
8. Da Cruz Gomes, A.A.; Grassi, E.N.D.; Da Silva, P.C.S.; De Araújo, C.J. Mechanical Behavior of a NiTi Superelastic Bone Plate Obtained by Investment Casting Assisted by Additive Manufacturing. *Smart Mater. Struct.* **2020**, *30*, 025009. [[CrossRef](#)]
9. de Souza, E.F.; da Silva, P.C.S.; Grassi, E.N.D.; de Araújo, C.J.; de Lima, A.G.B. Critical Frequency of Self-Heating in a Superelastic Ni-Ti Belleville Spring: Experimental Characterization and Numerical Simulation. *Sensors* **2021**, *21*, 7140. [[CrossRef](#)]
10. Chaudhari, R.; Kevalramani, A.; Vora, J.; Khanna, S.; Patel, V.K.; Pimenov, D.Y.; Giasin, K. Parametric Optimization and Influence of Near-Dry WEDM Variables on Nitinol Shape Memory Alloy. *Micromachines* **2022**, *13*, 1026. [[CrossRef](#)]
11. Yahia, L.L. *Yahia Shape Memory Implants*; Springer: Berlin, Germany, 2000; ISBN 9783642641183.
12. Wagner, M.F.X.; Dey, S.R.; Gugel, H.; Frenzel, J.; Somsen, C.; Eggeler, G. Effect of Low-Temperature Precipitation on the Transformation Characteristics of Ni-Rich NiTi Shape Memory Alloys during Thermal Cycling. *Intermetallics* **2010**, *18*, 1172–1179. [[CrossRef](#)]
13. Kim, J.I.; Liu, Y.; Miyazaki, S. Ageing-Induced Two-Stage R-Phase Transformation in Ti-50.9 at.% Ni. *Acta Mater.* **2004**, *52*, 487–499. [[CrossRef](#)]
14. Saedi, S.; Turabi, A.S.; Andani, M.T.; Haberland, C.; Karaca, H.; Elahinia, M. The Influence of Heat Treatment on the Thermo-mechanical Response of Ni-Rich NiTi Alloys Manufactured by Selective Laser Melting. *J. Alloys Compd.* **2016**, *677*, 204–210. [[CrossRef](#)]
15. Karimzadeh, M.; Aboutalebi, M.R.; Salehi, M.T.; Abbasi, S.M.; Morakabati, M. Effects of Thermomechanical Treatments on the Martensitic Transformation and Critical Stress of Ti-50.2 at.% Ni Alloy. *J. Alloys Compd.* **2015**, *637*, 171–177. [[CrossRef](#)]
16. Todoroki, T.; Tamura, H. Effect of Heat Treatment after Cold Working on the Phase Transformation in TiNi Alloy. *Trans. Jpn. Inst. Met.* **1987**, *28*, 83–94. [[CrossRef](#)]
17. Nam, T.; Chung, D.; Noh, J.; Lee, H. Phase Transformation Behavior and Wire Drawing Properties of Ti-Ni-Mo Shape Memory Alloys. *J. Mater. Sci.* **2001**, *6*, 4181–4188. [[CrossRef](#)]
18. Manjeri, R.M.; Norwich, D.; Sczerzenie, F.; Huang, X.; Long, M.; Ehrlinspiel, M. A Study of Thermo-Mechanically Processed High Stiffness NiTiCo Shape Memory Alloy. *J. Mater. Eng. Perform.* **2016**, *25*, 894–900. [[CrossRef](#)]
19. Hsieh, S.F.; Wu, S.K. A Study on the Nickel-Rich Ternary Ti-Ni-Al Shape Memory Alloys. *J. Mater. Sci.* **1997**, *32*, 989–996. [[CrossRef](#)]
20. Fukuda, T.; Todai, M.; Kakeshita, T. Isothermal Martensitic Transformation of the R-Phase in a Ti-44Ni-6Fe at.% Alloy. *Scr. Mater.* **2013**, *69*, 239–241. [[CrossRef](#)]
21. Xi, R.; Jiang, H.; Li, G.; Zhang, Z.; Zhao, G.; Vanmeensel, K.; Kustov, S.; Van Humbeeck, J.; Wang, X. Effect of Fe Addition on the Microstructure, Transformation Behaviour and Superelasticity of NiTi Alloys Fabricated by Laser Powder Bed Fusion. *Virtual Phys. Prototyp.* **2023**, *18*, e2126376. [[CrossRef](#)]
22. Mohammed, S.H.; Aljubouri, A.A.; Mohammed, M.A. The Effect of Cobalt Element Addition on the Characteristics of Equiatomic NiTi Shape Memory Alloy. *J. Phys. Conf. Ser.* **2020**, *1660*, 012038. [[CrossRef](#)]
23. Kim, Y.W. Martensitic Transformation Behavior and Mechanical Properties of Highly Porous Ti-Ni-Mo Scaffolds. *J. Alloys Compd.* **2020**, *821*, 153220. [[CrossRef](#)]
24. Nam, T.; Chung, D.; Kim, J.; Kang, S. Phase Transformation Behaviors and Shape Memory Characteristics of Ti-Ni-Mo Alloys. *Mater. Lett.* **2002**, *52*, 234–239. [[CrossRef](#)]
25. Liu, F.; Ding, Z.; Li, Y.; Xu, H. Phase Transformation Behaviors and Mechanical Properties of TiNiMo Shape Memory Alloys. *Intermetallics* **2005**, *13*, 357–360. [[CrossRef](#)]
26. Kim, Y.W. Martensitic Transformation Behaviors of Rapidly Solidified Ti-Ni-Mo Powders. *Mater. Res. Bull.* **2012**, *47*, 2956–2960. [[CrossRef](#)]
27. Kim, Y.W.; Jo, B.G.; Young, S.; Nam, T.H. Shape Memory Characteristics of Porous Ti-Ni-Mo Alloys Prepared by Solid State Sintering. *Mater. Res. Bull.* **2016**, *82*, 45–49. [[CrossRef](#)]
28. Medeiros, M.A.R.; de Araújo, C.J. Thermal, Microstructural and Elastic Modulus Behavior of Ti50Ni50-xNbx (x = 0–25%at) Shape Memory Alloys Obtained by Plasma Arc Melting. *J. Alloys Compd.* **2021**, *866*, 158970. [[CrossRef](#)]
29. *ASTM-B600-11R17*; Standard Guide for Descaling and Cleaning Titanium and Titanium Alloy Surfaces. Annual Book of ASTM; ASTM International: West Conshohocken, PA, USA, 2017; pp. 1–3.
30. de Araújo, C.J.; Gomes, A.A.C.; Silva, J.A.; Cavalcanti, A.J.T.; Reis, R.P.B.; Gonzalez, C.H. Fabrication of Shape Memory Alloys Using the Plasma Skull Push-Pull Process. *J. Mater. Process. Technol.* **2009**, *209*, 3657–3664. [[CrossRef](#)]
31. *ASTM-E407-99*; Standard Practice for Microetching Metals and Alloys. Annual Book of ASTM; ASTM International: West Conshohocken, PA, USA, 2003; pp. 1–15.
32. *ASTM-F2004-05*; Standard Test Method for Transformation Temperature of Nickel-Titanium Alloys by Thermal Analysis. ASTM International: West Conshohocken, PA, USA, 2010; p. 4.
33. *ASTM-F2129-08*; Standard Test Method for Conducting Cyclic Potentiodynamic Polarization Measurements to Determine the Corrosion Susceptibility of Small Implant Devices. ASTM International: West Conshohocken, PA, USA, 2015; p. 9.
34. Popov, B.N. Basics of Corrosion Measurements. In *Corrosion Engineering*; Elsevier: Amsterdam, The Netherlands, 2015; pp. 181–237, ISBN 978-0-444-62722-3.

35. Ramos, A.P.; de Castro, W.B.; Costa, J.D.; de Santana, R.A.C. Influence of Zirconium Percentage on Microhardness and Corrosion Resistance of Ti₅₀Ni_{50-x}Zr_x Shape Memory Alloys. *Mater. Res.* **2019**, *22*, e20190118. [[CrossRef](#)]
36. Hastuti, K.; Hamzah, E.; Hashim, J. Effect of Ageing Treatment on the Microstructures of Ti-50.7at.%Ni Shape Memory Alloy. *Adv. Mater. Res.* **2013**, *686*, 180–191. [[CrossRef](#)]
37. Zhang, D.T.; Guo, B.; Tong, Y.X.; Tian, B.; Li, L.; Zheng, Y.F.; Gunderov, D.V.; Valiev, R.Z. Effect of Annealing Temperature on Martensitic Transformation of Ti_{49.2}Ni_{50.8} Alloy Processed by Equal Channel Angular Pressing. *Trans. Nonferrous Met. Soc. China* **2016**, *26*, 448–455. [[CrossRef](#)]
38. Toro, A.; Zhou, F.; Wu, M.H.; Van Geertruyden, W.; Misiólek, W.Z. Characterization of Non-Metallic Inclusions in Superelastic NiTi Tubes. *J. Mater. Eng. Perform.* **2009**, *18*, 448–458. [[CrossRef](#)]
39. Rahim, M.; Frenzel, J.; Frotscher, M.; Pfetzinger-Micklich, J.; Steegmüller, R.; Wohlschlägel, M.; Mughrabi, H.; Eggeler, G. Impurity Levels and Fatigue Lives of Pseudoelastic NiTi Shape Memory Alloys. *Acta Mater.* **2013**, *61*, 3667–3686. [[CrossRef](#)]
40. Mentz, J.; Frenzel, J.; Wagner, M.F.X.; Neuking, K.; Eggeler, G.; Buchkremer, H.P.; Stöver, D. Powder Metallurgical Processing of NiTi Shape Memory Alloys with Elevated Transformation Temperatures. *Mater. Sci. Eng. A* **2008**, *491*, 270–278. [[CrossRef](#)]
41. Kai, W.Y.; Chang, K.C.; Wu, H.F.; Chen, S.W.; Yeh, A.C. Formation Mechanism of Ni₂Ti₄O_x in NITI Shape Memory Alloy. *Materialia* **2019**, *5*, 100194. [[CrossRef](#)]
42. Hsieh, S.F.; Hsue, A.W.J.; Chen, S.L.; Lin, M.H.; Ou, K.L.; Mao, P.L. EDM Surface Characteristics and Shape Recovery Ability of Ti_{35.5}Ni_{48.5}Zr₁₆ and Ni₆₀Al_{24.5}Fe_{15.5} Ternary Shape Memory Alloys. *J. Alloys Compd.* **2013**, *571*, 63–68. [[CrossRef](#)]
43. Swain, B.; Chatterjee, S.; Mohapatra, S.S.; Behera, A. Mechanical Properties Evaluation and Parametric Optimization of Atmospheric Plasma Spray NiTi Coating. *J. Mater. Eng. Perform.* **2022**, *31*, 8270–8284. [[CrossRef](#)]
44. Ifeolu Odetola, P.; Popoola, A.P.I.; Ajenifuja, E.; Popoola, O. Effects of Temperature on the Microstructure and Physico-Mechanical Properties of TiNiAl-SiC Composite by Spark Plasma Sintering Technique. *Mater. Res. Express* **2019**, *6*, 085802. [[CrossRef](#)]
45. Chan, C.W.; Man, H.C.; Yue, T.M. Effect of Post-Weld Heat-Treatment on the Oxide Film and Corrosion Behaviour of Laser-Welded Shape Memory NiTi Wires. *Corros. Sci.* **2012**, *56*, 158–167. [[CrossRef](#)]
46. Rajadurai, M.; Muthuchamy, A.; Annamalai, A.R.; Agrawal, D.K.; Jen, C.P. Effect of Molybdenum (Mo) Addition on Phase Composition, Microstructure, and Mechanical Properties of Pre-Alloyed Ti6Al4v Using Spark Plasma Sintering Technique. *Molecules* **2021**, *26*, 2894. [[CrossRef](#)]
47. Xu, H.B.; Meng, L.J.; Xu, J.; Li, Y.; Zhao, X.Q. Mechanical Properties and Oxidation Characteristics of TiNiAl(Nb) Intermetallics. *Intermetallics* **2007**, *15*, 778–782. [[CrossRef](#)]
48. Marattukalam, J.J.; Balla, V.K.; Das, M.; Bontha, S.; Kalpathy, S.K. Effect of Heat Treatment on Microstructure, Corrosion, and Shape Memory Characteristics of Laser Deposited NiTi Alloy. *J. Alloys Compd.* **2018**, *744*, 337–346. [[CrossRef](#)]
49. Gale, W.F.; Totemeier, T.C. *Smithells Metals Reference Book*; Elsevier: Amsterdam, The Netherlands, 2003; ISBN 0080480969.
50. Klopotov, A.; Gunther, V.; Marchenko, E.; Baigonakova, G.; Chekalkin, T.; Kim, J.S.; Kang, J.H. Impact of Annealing Temperature on Martensite Transformations and Structure of Quaternary Ti₅₀Ni_{47.7}Mo_{0.3}V₂ Alloy. *Adv. Mater. Lett.* **2016**, *8*, 122–127. [[CrossRef](#)]
51. Chen, Y.; Jiang, H.C.; Liu, S.W.; Rong, L.J.; Zhao, X.Q. The Effect of Mo Additions to High Damping Ti-Ni-Nb Shape Memory Alloys. *Mater. Sci. Eng. A* **2009**, *512*, 26–31. [[CrossRef](#)]
52. Jiang, H.C.; Rong, L.J. Microstructures and Mechanical Properties of Porous Ti₅₁Ni_(49-x)Mo_x Shape Memory Alloys. *Mater. Sci. Forum* **2007**, *546–549*, 2127–2132. [[CrossRef](#)]
53. Pan, G.; Cao, Z.; Shi, J.; Wei, M.; Xu, L.; Meng, X. Different Mechanical Response of TiNi Film Induced by the Shape of Indenter during Nanoindentation. *Sens. Actuators A Phys.* **2014**, *217*, 75–80. [[CrossRef](#)]
54. Huang, X.; Nohava, J.; Zhang, B.; Ramirez, A.G. Nanoindentation of NiTi Shape Memory Thin Films at Elevated Temperatures. *Int. J. Smart Nano Mater.* **2011**, *2*, 39–49. [[CrossRef](#)]
55. Birlik, I.; Ak Azem, N.F.; Toparli, M.; Celik, E.; Koc Delice, T.; Yildirim, S.; Bardakcioglu, O.; Dikici, T. Preparation and Characterization of Ni-TiO₂ Nanocomposite Coatings Produced by Electrodeposition Technique. *Front. Mater.* **2016**, *3*, 46. [[CrossRef](#)]
56. Ozaki, T.; Matsumoto, H.; Watanabe, S.; Hanada, S. Beta Ti Alloys with Low Young's Modulus. *Mater. Trans.* **2004**, *45*, 2776–2779. [[CrossRef](#)]
57. Zhao, T.; Li, Y.; Xiang, Y.; Zhao, X.; Zhang, T. Surface Characteristics, Nano-Indentation and Corrosion Behavior of Nb Implanted NiTi Alloy. *Surf. Coat. Technol.* **2011**, *205*, 4404–4410. [[CrossRef](#)]
58. Shayesteh Moghaddam, N.; Taheri Andani, M.; Amerinatanzi, A.; Haberland, C.; Huff, S.; Miller, M.; Elahinia, M.; Dean, D. Metals for Bone Implants: Safety, Design, and Efficacy. *Biomater. Rev.* **2016**, *1*, 1. [[CrossRef](#)]
59. Rho, J.Y.; Roy, M.E.; Tsui, T.Y.; Pharr, G.M. Elastic Properties of Microstructural Components of Human Bone Tissue as Measured by Nanoindentation. *J. Biomed. Mater. Res.* **1999**, *45*, 48–54. [[CrossRef](#)]
60. Zinelis, S.; Eliades, T.; Eliades, G. A Metallurgical Characterization of Ten Endodontic Ni-Ti Instruments: Assessing the Clinical Relevance of Shape Memory and Superelastic Properties of Ni-Ti Endodontic Instruments. *Int. Endod. J.* **2010**, *43*, 125–134. [[CrossRef](#)] [[PubMed](#)]
61. He, G.; Hagiwara, M. Bimodal Structured Ti-Base Alloy with Large Elasticity and Low Young's Modulus. *Mater. Sci. Eng. C* **2005**, *25*, 290–295. [[CrossRef](#)]
62. John, R.; Umamaheshwari, M. Ductility Reduction upon Cobalt Substitution in B2 NiTi. *Comput. Mater. Sci.* **2023**, *220*, 112049. [[CrossRef](#)]

63. Li, S.; Li, J.; Sun, G.; Deng, D. Modeling of Welding Residual Stress in a Dissimilar Metal Butt-Welded Joint between P92 Ferritic Steel and SUS304 Austenitic Stainless Steel. *J. Mater. Res. Technol.* **2023**, *23*, 4938–4954. [[CrossRef](#)]
64. De Oliveira, A.G.; Giacomelli, F.C.; Giacomelli, C.; Spinelli, A. Microstructure and Surface Composition Effects on the Transpassivation of NiTi Wires for Implant Purposes. *J. Braz. Chem. Soc.* **2005**, *16*, 131–138. [[CrossRef](#)]
65. Saebnoori, E.; Shahrabi, T.; Sanjabi, S.; Ghaffari, M.; Barber, Z.H. Surface Characteristics and Electrochemical Behaviour of Sputter-Deposited NiTi Thin Film. *Philos. Mag.* **2015**, *95*, 1696–1716. [[CrossRef](#)]
66. Li, K.; Li, Y.; Huang, X.; Gibson, D.; Zheng, Y.; Liu, J.; Sun, L.; Fu, Y.Q. Surface Microstructures and Corrosion Resistance of Ni-Ti-Nb Shape Memory Thin Films. *Appl. Surf. Sci.* **2017**, *414*, 63–67. [[CrossRef](#)]
67. Mareci, D.; Chelariu, R.; Bolat, G.; Cailean, A.; Grancea, V.; Sutiman, D. Electrochemical Behaviour of Ti Alloys Containing Mo and Ta as β -Stabilizer Elements for Dental Application. *Trans. Nonferrous Met. Soc. China* **2013**, *23*, 3829–3836. [[CrossRef](#)]
68. Zhou, Y.L.; Luo, D.M. Corrosion Behavior of Ti-Mo Alloys Cold Rolled and Heat Treated. *J. Alloys Compd.* **2011**, *509*, 6267–6272. [[CrossRef](#)]
69. Abdel Hamid, Z.; Hassan, H.B. Influence of Electrodeposition Parameters on the Characteristics of NiMoP Film. *Surf. Coat. Technol.* **2012**, *212*, 37–45. [[CrossRef](#)]
70. Wu, Y.; He, H. Electrodeposited Nickel–Iron–Carbon–Molybdenum Film as Efficient Bifunctional Electrocatalyst for Overall Water Splitting in Alkaline Solution. *Int. J. Hydrogen Energy* **2019**, *44*, 1336–1344. [[CrossRef](#)]
71. Liu, K.; Zhang, H.; Xiu, M.; Huang, Z.; Huang, H.; Xu, Y.; Zhou, R.; Xiao, H. Microstructure Evolution, Mechanical Properties, and Corrosion Resistance of Hot Rolled and Annealed Ti-Mo-Ni Alloy. *Metals* **2023**, *13*, 566. [[CrossRef](#)]

Disclaimer/Publisher’s Note: The statements, opinions and data contained in all publications are solely those of the individual author(s) and contributor(s) and not of MDPI and/or the editor(s). MDPI and/or the editor(s) disclaim responsibility for any injury to people or property resulting from any ideas, methods, instructions or products referred to in the content.